# Gold−Copper Nanoparticles: Nanostructural Evolution and Bifunctional Catalytic Sites

Jun Yin,[†] Shiyao Shan,[†] Lefu Yang,[†,‡] Derrick Mott,[†,#] Oana Malis,[§] Valeri Petkov,[∥] Fan Cai,[‡] Mei Shan Ng,[†] Jin Luo,[†] Bing H. Chen,[‡] Mark Engelhard,[⊥] and Chuan-Jian Zhong*,[†]

[†] Department of Chemistry, State University of New York at Binghamton, Binghamton, New York 13902, United States
[‡] College of Chemistry and Chemical Engineering, Xiamen University, Xiamen 361005, China
[§] Physics Department, Purdue University, West Lafayette, Indiana 47907, United States
[∥] Department of Physics, Central Michigan University, Mount Pleasant, Michigan 48859, United States
[⊥] EMSL, Pacific Northwest National Laboratory, Richland, Washington 99352, United States

Ⓢ Supporting Information

**ABSTRACT:** Understanding of the atomic-scale structure is essential for exploiting the unique catalytic properties of any nanoalloy catalyst. This report describes novel findings of an investigation of the nanoscale alloying of gold−copper (AuCu) nanoparticles and its impact on the surface catalytic functions. Two pathways have been explored for the formation of AuCu nanoparticles of different compositions, including wet chemical synthesis from mixed Au- and Cu-precursor molecules, and nanoscale alloying via an evolution of mixed Au- and Cu-precursor nanoparticles near the nanoscale melting temperatures. For the evolution of mixed precursor nanoparticles, synchrotron X-ray-based in situ real-time XRD was used to monitor the structural changes, revealing nanoscale alloying and reshaping toward an fcc-type nanoalloy (particle or cube) via a partial melting−resolidification mechanism. The nanoalloys supported on carbon or silica were characterized by in situ high-energy XRD/atomic pair disributoin function (PDF) analyses, revealing an intriguing lattice "expanding−shrinking" phenomenon depending on whether the catalyst is thermochemically processed under an oxidative or reductive atmosphere. This type of controllable structural changes is found to play an important role in determining the catalytic activity of the catalysts for carbon monoxide oxidation reaction. The tunable catalytic activities of the nanoalloys under thermochemically oxidative and reductive atmospheres are also discussed in terms of the bifunctional sites and the surface oxygenated metal species for carbon monoxide and oxygen activation.

KEYWORDS: gold−copper nanoalloys, nanoparticles, molecule-solid duality, catalysts, thermochemical processing, CO oxidation
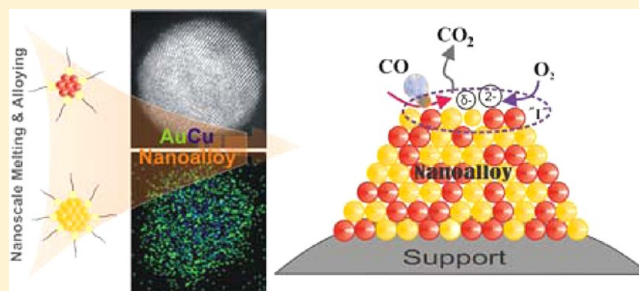
## INTRODUCTION

Understanding of the atomic-scale structure is essential for exploiting the unique catalytic properties of nanoalloy based catalysts. This understanding can be achieved by obtaining knowledge of the alloy formation process and the evolution of surface sites under reactive conditions. While the study of nanoscale alloy formation has been largely focused on the bottom-up approach, that is, the synthesis from the mixed metal precursors, recently, the focus has shifted to revealing the structural evolution of preformed metal or alloy nanoparticles.[1−4] One of the fundamental differences of metal particles confined to nanoscale dimensions from their bulk counterparts is the molecule-like chemical reactivity and the solid-like melting behavior.[5,6] This type of "molecule-solid duality" concept is applicable to multicomponent nanoscale systems (e.g., binary, ternary, etc.) in terms of alloying characteristics. Moreover, since metallic nanoparticles melt at lower temperatures than their bulk counterparts, the surface melting could take place at even lower temperatures, leading to

an increased propensity of the nanoparticle surface atoms to detach, diffuse, and reattach. The knowledge of the dependency of surface melting on the size and strain[7] has been so far largely limited to unary metal particles. For small clusters of Au, Pt, Ag, and Cu with noncrystallographic 5-fold symmetry and irregular interatomic ordering, it is not well understood how such "molecule-solid" duality operates in conjunction with the particle size, shape, composition, and structure type. Consider a binary system of Cu and Au nanoclusters/nanoparticles in a solution or on a solid substrate. The structural evolution at or near their melting temperatures is different from the evolution of unary nanocluster systems. For example, the evolution of thiolate-capped Cu (<10) nanoclusters forms $Cu_2S$ nanodiscs,[3] whereas that of Au (<2-nm) forms larger-sized Au nanoparticles.[1,2] Indeed, recently, we demonstrated resizing,

reshaping, and alloying of a binary system of Au and Cu nanoparticles near the melting temperature.[4] This type of alloying differs from most wet chemical synthesis approaches such as reduction of $Cu^{2+}$ with mixed gold precursors,[8] seed−based diffusion route by heating a mixture of Cu(II) and Au seeds,[9] reduction of Cu(II) and Au(III),[10] and other wet chemical reductions.[11,12]

Among different bimetallic alloy nanoparticle catalysts, AuCu catalysts have recently attracted interests for catalytic oxidation of CO, benzyl alcohol, and propene[12−16] and for partial oxidation of methanol to produce hydrogen fuels.[17] Some intriguing structural evolution of AuCu catalysts have been shown under catalytic reaction conditions. For example, an oxidation treatment of silica supported AuCu catalysts at a temperature (500 °C) was shown to produce Au and amorphous CuO heterostructures (Au-CuO/SiO$_2$) and to increase the catalytic activity for CO oxidation reaction, whereas the reduction of the Au-CuO/SiO$_2$ by hydrogen deactivated the catalyst.[18a] In another example, the treatment of Au−Cu/SBA-15 catalysts for preferential oxidation of CO in H$_2$-rich gas was revealed to influence the catalytic activity in a similar fashion,[18b] where the oxidation of the catalyst led to a phase segregation into Au and CuO$_x$ and to increase the activity, whereas the reduction led to an alloy formation that deactivates the activity. While these findings are very interesting, the understanding of how the synthesis and processing parameters control alloying or phase segregation that influences the activation of molecular oxygen and how the atomic-scale structural and chemical ordering/disordering in the alloy nanoparticles under the oxidative/reductive conditions correlate with the catalytic activity remains highly elusive. We also note that recent studies of small copper-dopped gold cage nanoclusters based on photoelectron spectroscopy and density functional theory calculations have revealed intriguing changes in their structural, electronic, and magnetic properties,[19a−e] providing useful information for an in-depth understanding of AuCu nanoclusters.

This report presents the results of an investigation of the atomic-scale structure and its evolution of metal and alloy nanoparticles under controlled thermochemical conditions, focusing on finding a correlation between the structural evolution and the nature of the surface catalytic sites of AuCu nanoparticles. Scheme 1 illustrates structural evolution of the nanoalloy by two distinctive pathways: (i) wet chemical reduction of mixed metal-precursor molecules (left), and (ii) cross-reactive processing of a binary solution of metal nanoparticles (right). In both cases, the "molecule-solid" duality concept is exploited in the cross reactivity of Cu- and Au-precursor molecules or Au and Cu nanoclusters/nanoparticles at or near the nanoscale melting temperature. The emphasis is the understanding of how this type of duality concept operates in controlling the formation of nanoalloy and how their atomic-scale structure evolves under controlled thermochemical conditions toward the creation of bifunctional catalytic sites. The oxidation reaction of carbon monoxide with oxygen is used as a probe to the catalytic activity. As will be shown in this report, synchrotron X-ray-based in situ XRD can provide important insights, especially for understanding the role of the nanostructural evolution in determining the surface catalytic functions of the nanoalloy.

**Scheme 1. Illustrations of Two Strategies for Synthesis and Processing of AuCu Alloy Nanoparticles, Bottom-up Reduction of the Two Metal Precursors (left) and Cross-Reactive Evolution of a Binary Solution of Cu and Au Nanoparticles at or near the Nanoscale Melting Temperature (right), towards a Catalyst with Bifunctional Catalytic Sites (bottom)$^a$**
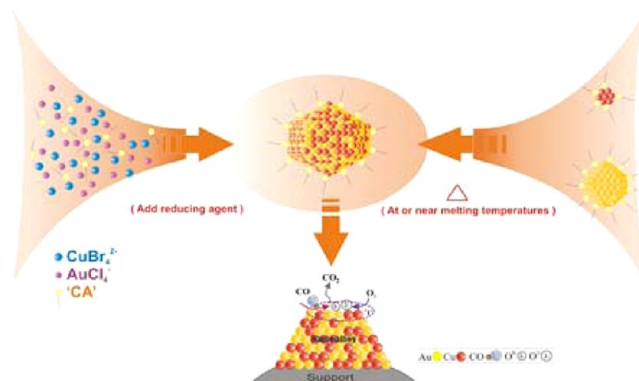


$^a$Note that atoms, particles, and capping molecules (CA) are not drawn to scale.

## ■ EXPERIMENTAL SECTION

**Chemicals.** Copper(II) chloride dihydrate (CuCl$_2$·2H$_2$O 99% pure) was obtained from Lancaster Synthesis. Hydrogen tetrachloroaurate (III) hydrate (HAuCl$_4$) was obtained from Strem Chemicals. Tetra-$n$-octylammonium bromide (TOABr, 98%) was obtained from Alfa Aesar. 1−Decanethiol (96%), potassium bromide (99%), sodium borohydride (99%), hexane, toluene, and other common solvents used were obtained from Aldrich. Water was purified with a Millipore Direct-Q system with a final resistance of 18.2 M Ohm.

**Synthesis of Cu and Au Nanoparticles.** The synthesis of decanethiolate (DT) capped Au nanoparticles followed the modified two-phase reduction method.[20,21] The synthesis of decanethiolate-capped Cu nanoclusters was recently described.[22] Briefly, CuCl$_2$ was dissolved in water in the presence of 4.3 M KBr. $Cu^{2+}$ was converted to CuBr$_4{}^{2−}$, which was transferred from aqueous phase to the organic phase by adding a solution of TOABr in toluene (40 mL toluene, 180 mM TOABr). After 20 min of vigorous stirring, the aqueous solution was removed. The toluene solution was stirred under argon purge to eliminate oxygen from the system. 0.36 mL of decanethiol was added, and the solution was stirred for another 1 h, resulting in the color change of solution from dark purple to a light green. NaBH$_4$ solution (25 mL, 0.4 M) was added dropwise. After reaction for 2 h under argon, the aqueous layer was removed, and the solution was stirred overnight.

**Synthesis of AuCu Alloy Nanoparticles from Mixed Au- and Cu-Precursor Molecules.** The synthesis of AuCu nanoparticles was following the modified two-phase reduction method.[20,21] Briefly, CuCl$_2$ and HAuCl$_4$ were dissolved in water in a controlled ratio. With the presence of 4.3 M KBr, $Cu^{2+}$ is converted to CuBr$_4{}^{2−}$, which was transferred from aqueous phase to the organic phase by adding a solution of TOABr in toluene (40 mL toluene, 180 mM TOABr). After 20 min of vigorous stirring, the aqueous solution was removed. The toluene solution was stirred under argon purge to eliminate all oxygen from the system. 0.36 mL decanethiol was added, and the solution was stirred for another 1 h. NaBH$_4$ solution (25 mL, 0.4 M) was added dropwise. The solution was stirred for 4 h. Thermal processing of as-synthesized AuCu nanoparticles was performed by heating a concentrated solution (~15×) under a temperature of 150−170 °C for 2−3 h.

**Synthesis of AuCu Alloy Nanoparticles from Mixed Cu- and Au-Precursor Nanoparticles/Nanoclusters.** The solutions of the as-synthesized Au nanoparticles and Cu nanoclusters were mixed in a controlled ratio.[2,23] The mixed solution was then concentrated by a
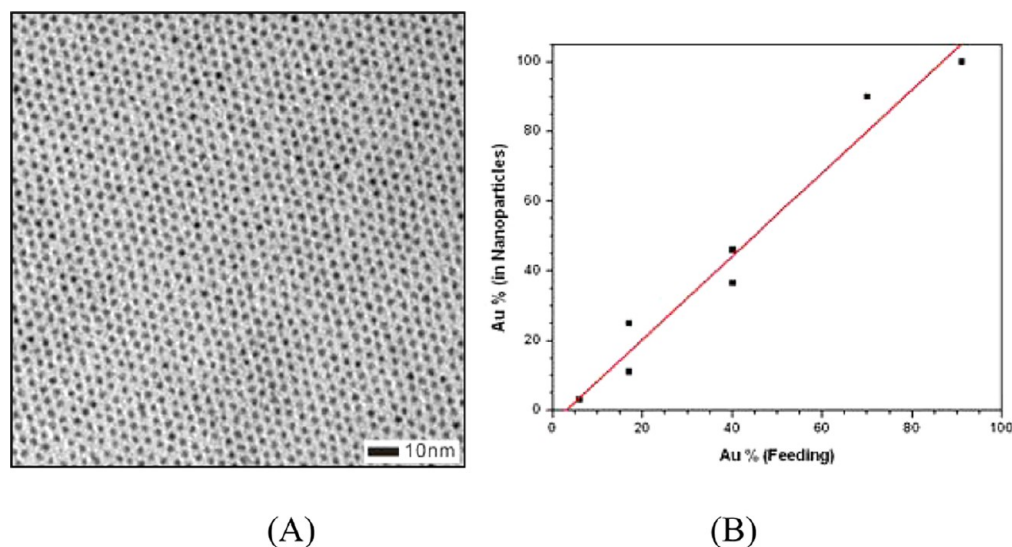
**Figure 1.** (A) TEM image for a sample of as-synthesized $Au_{46}Cu_{54}$ (2.2 ± 0.3 nm) nanoparticles. (B) Correlation between the Au composition in nanoparticles (from ICP-OES analysis) and the synthetic feeding composition. The solid line represents the linear fitting to the experimental data (slope: 1.2, $R^2$ = 0.966).

factor of ~15 in a glass reactor and was kept in an oven under controlled temperature (150−170 °C) and reaction time. 156 °C was identified as an optimal temperature for forming nanocubes by examining a series of temperatures ranging from 150 to 172 °C.

**Instrumentation and Measurements.** The nanoparticles were characterized using traditional small angle X-ray scattering (SAXS) and wide angle X-ray scattering (WAXS), transmission electron microscopy (TEM), and X-ray photoelectron spectroscopy (XPS). Traditional SAXS and WAXS patterns of copper nanoparticle suspensions were recorded at room temperature with Cu Kα radiation from a 1.2 kW rotating anode X-ray generator (007 HF, Rigaku Denki Co. Ltd., Japan), and both the two-dimensional multiwire detector and the image plate were used for low and high scattering angle. The sample−detector distance of 1.5 mm (SAXS) and 34.8 mm (WAXS), which allowed a "q range" from 0.006 to 0.12 $Å^{-1}$ and 0.1 to 4 $Å^{-1}$ [$q = 4\pi/\lambda \sin(\theta/2)$, where $\lambda$ is X-ray wavelength and $\theta$ is scattering angle]. The scattering intensity after subtraction of the empty cell and background was circularly averaged.

Maldi-TOF mass spectra were collected with an Ettan instrument from GE Healthcare operated in reflection mode with the accelerating voltage held constant at 20 kV. The calibration standards used were proteins of molecular weight 1046.54 and 2464.91. The matrix used for the sample was DCTB (*trans*-2-[3-(4-*tert*-butylphenyl)-2-methyl-2-propenylidene]-malononitrile), while that used for calibrants was sinapinic acid.

Acid digestates of samples were analyzed using inductively coupled plasma optical emission spectroscopy (ICP-OES), which was performed using a Perkin-Elmer 2000 DV ICP-OES utilizing a cross-flow nebulizer with the following parameters: plasma 18.0 L Ar(g)/min; auxiliary 0.3 L Ar(g)/min; nebulizer 0.73 L Ar(g)/min; power 1500 W; peristaltic pump rate 1.40 mL/min. Reported values <1.0 mg/L were analyzed using a Meinhardt nebulizer coupled to a cyclonic spray chamber to increase analyte sensitivity at the following parameters: 18.0 L Ar(g)/min; auxiliary 0.3 L Ar(g)/min; nebulizer 0.63 L Ar(g)/min; power 1500 W; peristaltic pump rate 1.00 mL/min. Elemental concentrations were determined by measuring one or more emission lines (nm) to check for interferences. The nanoparticle samples were dissolved in concentrated aqua regia and then diluted to concentrations in the range of 1 to 50 ppm for analysis. Multipoint calibration curves were made from dissolved standards with concentrations from 0 to 50 ppm in the same acid matrix as the unknowns. Laboratory check standards were analyzed after measuring 6 or 12 samples, and the instrument was recalibratied if check standards were not within ±5% of the initial concentration. The

instrument reproducibility (*n* = 10) was determined using 1 mg/L elemental solutions ensuring <±2% error for all elements. The metal composition was expressed as atomic percentage of the elements in the nanoparticles.

High resolution TEM was carried out using a JEOL JEM 2010F with an acceleration voltage of 200 kV and a routine point-to-point resolution of 0.194 nm. TEM analysis was performed on an FEI Tecnai T12 Spirit Twin TEM/SEM electron microscope (120 kV). The nanoparticle samples were suspended in hexane solution and were drop cast onto a carbon-coated copper grid followed by solvent evaporation in air at room temperature.

XPS measurements were collected using a Physical Electronics Quantum 2000 scanning ESCA microprobe. This system uses a focused monochromatic Al Kα X-ray (1486.7 eV) source and a spherical section analyzer. The instrument has a 16 element multichannel detector. The X-ray beam used was a 100 W, 100 mm diameter that was rastered over a 1.3 mm by 0.2 mm rectangle on the sample. The X-ray beam is incident normal to the sample, and the photoelectron detector was at 45° off-normal. Wide scan data was collected using a pass energy of 117.4 eV. For the $Ag3d_{5/2}$ line, these conditions produce fwhm of better than 1.6 eV. High energy resolution photoemission spectra were collected using a pass energy of 46.95. For the $Ag3d_{5/2}$ line, these conditions produced fwhm of better than 0.77 eV. The binding energy (BE) scale was calibrated using the $Cu2p_{3/2}$ feature at 932.62 ± 0.05 eV and Au4f at 83.96 ± 0.05 eV for known standards. During the measurements the sample experienced variable degrees of charging. The vacuum chamber pressure during analysis was <1.3 × $10^{-6}$ Pa. Samples were dropped onto a molybdenum substrate and were allowed to dry. The C1s peak was used as an internal standard (284.9 eV) for the calibration of the binding energy.

In-house XRD data was collected on a Philips X'Pert diffractometer using Cu Kα radiation ($\lambda$ = 1.5418 Å). The measurements were done in reflection geometry and the diffraction (Bragg) angles $2\theta$ were scanned at a step of 0.025°. Each data point was measured for at least 20 s and several scans were taken of each sample measured.

The structural evolution of Au, Cu, and a physical mixture of Au and Cu nanoparticles subjected to heat treatment in the 25−225 °C temperature range was examined in situ, and in real-time with synchrotron-based X-ray diffraction. The experiment was performed at the National Synchrotron Light Source, Brookhaven National Laboratory, on beamline X20C using an X-ray energy of 6.9 keV (1.69 Å wavelength). A linear position sensitive detector was employed to simultaneously record the entire XRD pattern around
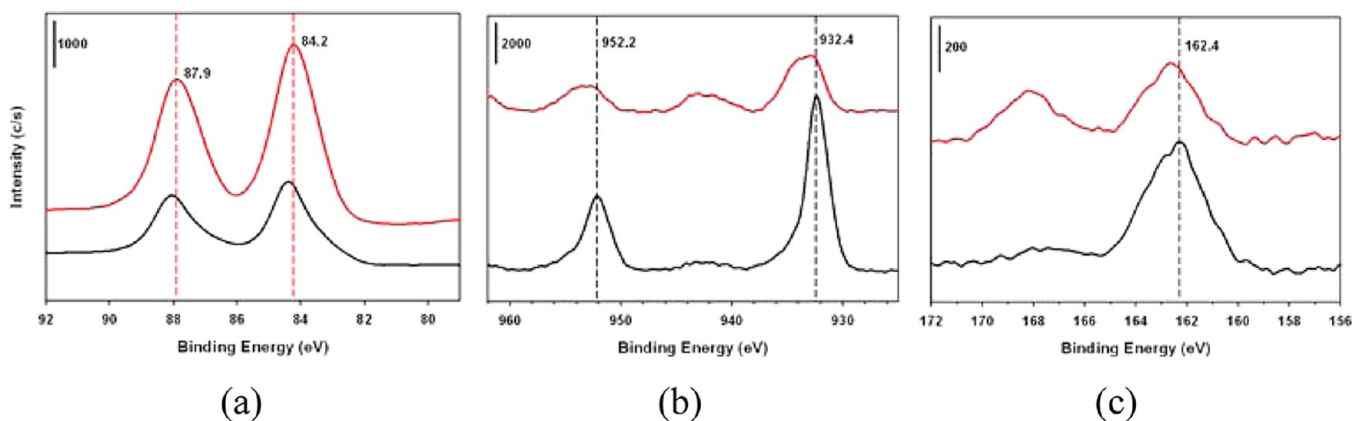
**Figure 2.** XPS spectra for as-synthesized $Au_{25}Cu_{75}$ (a, bottom black curve) and $Au_{46}Cu_{54}$ (b, top red curve) nanoparticles: (a) Au 4f; (b) Cu 2p; and (c) S 2p regions (all samples: C 1s peak = 284.8 eV).
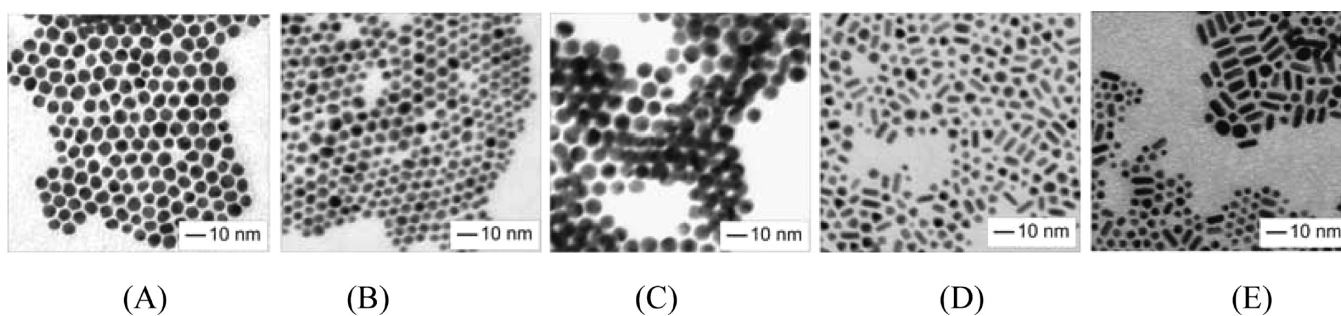


**Figure 3.** TEM micrographs of as-synthesized $Au_{46}Cu_{54}$ nanoparticles showing the particles size and shape evolution with temperature and TOABr concentration: (A) at 156 °C for 4 h (size 5.1 ± 0.4 nm), thermal evolution using 3× TOABr (B) at 156 °C, $t = 4$ h (size 5.3 ± 0.5 nm); (C) at 172 °C, $t = 4$ h (size 7.9 ± 0.5 nm) and using 1/3× TOABr (D) at 156 °C, 4 h (size 4.7 ± 0.6 nm (spheres)); (E) at 172 °C, 4 h (size 3.9 ± 0.3 nm (spheres)).

the face-centered cubic (111) and (200) peaks with two-second resolution time. The integrated intensity of the XRD peaks in the measured $2\theta$ range of 42−56° is proportional to the volume of the crystalline (fcc) phase, therefore providing information about the nanoparticle recrystallization process.

The structural change of the lattice under oxidative and reductive atmosphere was also characterized by in situ synchrotron high-energy XRD coupled to atomic pair disributoin function (PDF) analysis, which were correlated to the catalytic activities for CO oxidation. Those experiments were conducted at the beamline 11IDB at the Argonne National Laborarory using X-rays of energy 90.48 keV ($\lambda = 0.13072$ Å) and a sample cell described earlier.[24] The high-energy XRD data was reduced to the so-called structure factors, $S(q)$, and then Fourier transformed to the corresponding atomic PDFs $G(r)$, using the relationship:

$$G(r) = \frac{2}{\pi} \int_{q=0}^{q_{max}} q[S(q) - 1]\sin(qr) \, dq \qquad (1)$$

where $q_{max} = 25$ Å$^{-1}$ in the present experiments. The software RAD was used for this purpose.[25] Here, the wave vector $q$ is defined as $q = (4\pi \sin \theta)/\lambda$, where $\theta$ is half of the scattering angle and $\lambda$ is the wavelength of the X-rays used. Note, as derived, atomic PDF $G(r)$ is an experimental quantity that oscillate around zero and shows positive peaks at real space distances, $r$, where the local atomic density $\rho(r)$ exceeds the average one $\rho_o$. This behavior can be expressed by the equation $G(r) = 4\pi r\rho_o[\rho(r)/\rho_o - 1]$, which is the formal definition of the PDF $G(r)$. High-energy synchrotron XRD and atomic PDFs have already proven to be very efficient in studying the atomic-scale structure of nanosized particles.[26,27]

The catalytic activity of the catalysts for CO (1 vol % balanced by $N_2$) + $O_2$ (20 vol % balanced by $N_2$) reaction was measured using a customer-built system including a temperature-controlled reactor, gas

flow/mixing/injection controllers, and an online gas chromatograph (Shimadzu GC 8A) equipped with 5A molecular sieve and Porapak Q packed columns and a thermal conductivity detector. The catalytic activity for CO oxidation was determined by analyzing the composition of the tail gas effusing from the quartz microreactor packed with catalyst fixed bed.

## ■ RESULTS AND DISCUSSION

**1. Alloying via Metal Precursor Molecules and Thermal Processing.** *Morphology of As-Synthesized and Thermally Evolved AuCu Nanoparticles.* $Au_nCu_{100-n}$ nanoparticles with controllable bimetallic compositions and sizes have been synthesized by wet chemical reduction of the mixed Cu- and Au-precursor molecules. The exact bimetallic composition of the nanoparticles was determined by ICP analysis. Figure 1A shows a sample of as-synthesized $Au_{46}Cu_{54}$. The particles feature an average size of 2.2 ± 0.3 nm. As shown in Figure 1B, the controllability of the bimetallic composition in the AuCu nanoparticles is evidenced by an approximately 1:1 linear correlation between Au% in the bimetallic nanoparticles and in the synthetic feeding composition.

The relative surface bimetallic composition was also analyzed by XPS analysis of samples of as-synthesized $Au_{25}Cu_{75}$ and $Au_{46}Cu_{54}$ nanoparticles in Au 4f, Cu 2p, and S 2p regions (Figure 2). The Au 4f peaks shift to a slightly higher binding energy (BE, ~0.3 eV) as the percentage of Cu in the nanoparticles increases. In the Cu 2p region, the peaks contain a higher BE component for the AuCu nanoparticles with a lower percentage of Cu. The lower-BE peak in the S 2p region is characteristic of the capping thiolate species, which is largely
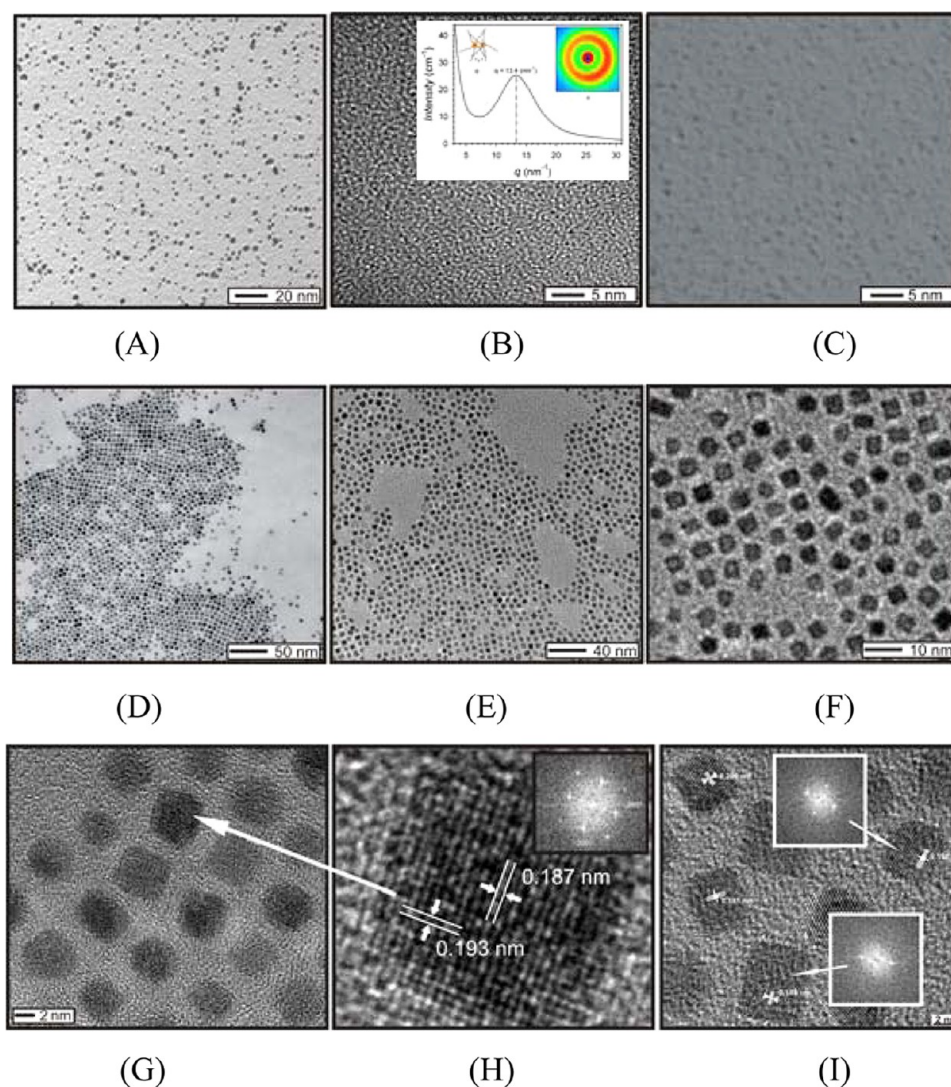
**Figure 4.** TEM micrographs: Au (A, 2.0 ± 0.7 nm), Cu nanoparticles (B, ~0.5 nm) capped with a DT monolayer, and Au nanoclusters capped by octadecanethiol (C, ~1 nm). Insert in B: A combined SAXS and WAXS spectrum of the nanoclusters, including a two−dimensional WAXS scattering patterns (radial averaging) and a scheme illustrating the interparticle distance (d) in the concentrated suspension);[3] $Au_{66}Cu_{34}$ alloy nanocubes formed from a binary solution of Cu nanoclusters and Au nanoparticles (D−F, Cu/Au molar ratio ~8, $T = 156$ °C, $t_h = 3$ h); HR-TEM and FFT pattern (insert) of $Au_{66}Cu_{34}$ alloy nanocubes formed from a binary solution of Cu nanoclusters and Au nanoparticles (G-I, Cu/Au molar ratio ~8, $T = 156$ °C, $t_h = 3$ h).

unchanged with different percentages of Cu. A higher-BE peak was detected for the nanoparticles, suggesting the presence of a fraction of oxidized thiolate species ($-SO_3^-$).

In comparison with the composition data determined by ICP (Figure 1B), the relative surface composition determined by XPS appeared to show a similar trend. However, a slightly higher concentration of Cu was detected by XPS, implying the possibility of a slight enrichment of Cu in the outer layer of the alloy nanoparticles. For example, for $Au_{46}Cu_{54}$ and $Au_{25}Cu_{75}$ as determined by ICP, the XPS-determined relative surface compositions were $Au_{37}Cu_{63}$ and $Au_{19}Cu_{81}$, respectively.

The thermal evolution of the morphology for the presynthesized AuCu nanoparticles were examined, as shown in Figure 3 for samples obtained under different thermal evolution conditions. The AuCu alloy nanoparticles obtained by the two-phase synthesis were thermally treated in the presence of TOABr. By thermal treatment of the as-synthesized $Au_{46}Cu_{54}$ nanoparticles (2.2 ± 0.3 nm) at 156 °C for 4 h, there is a clear size growth while retaining high monodispersity (5.1

± 0.4 nm) (Figure 3A). With the temperature increase, the particle size was observed to increase. When the temperature reached >182 °C, a significant aggregation of the particles occurs. The thermal evolution was further examined under different concentrations of TOABr (Figure 3B−E). By increasing the concentration of TOABr by a factor of 3 (Figure 3B−C), the morphology of the particles remained similar to that in the case of 1× TOABr. By using 1/3 times TOABr during the synthesis after thermal processing (Figure 3D, E), the observed morphologies suggested the formation of $Cu_2S$ nanodiscs (Figure 3D). Such features are significant upon reaching at higher temperatures (Figure 3E). The observations show that TOABr could play some role eventually leading to the formation of $Cu_2S$ and larger-sized Au nanoparticles in separate pathways.

The in-house XRD pattern obtained for the as-synthesized and thermally processed AuCu nanoparticles (Supporting Information Figure S1) indicated an fcc-type of alloy structure with a lattice constant (0.410 nm). In comparison with those
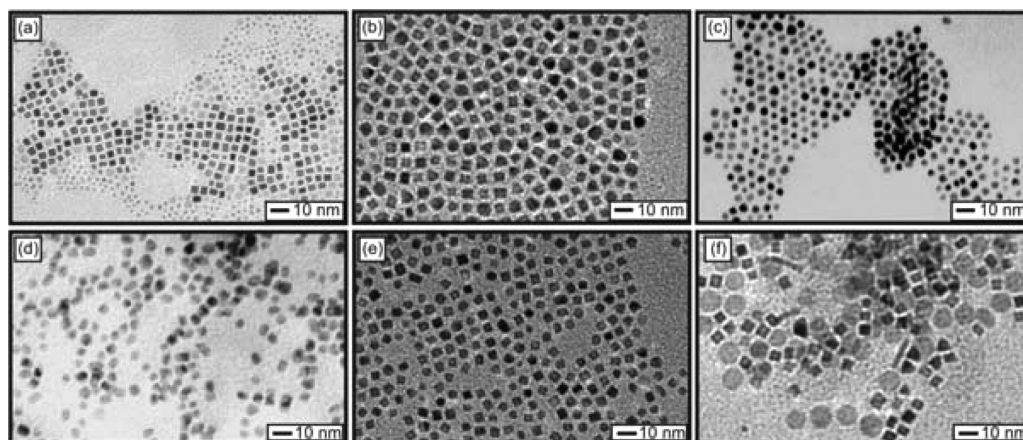
**Figure 5.** TEM micrographs comparing AuCu nanoparticles obtained under different conditions: (a) $t_h$ = 1.5 h (sizes ∼3.5 nm and ∼2 nm); (b) $t_h$ = 4.5 h (size ∼5.5 nm); (c) $t_h$ = 6 h, (size ∼4.5 nm) (a–c: $Au_{34}Cu_{66}$); (d) $t_h$ = 3 h (size ∼6 nm, $Au_{47}Cu_{53}$); (e) $t_h$ = 3 h (size ∼3.8 nm, $Au_{66}Cu_{34}$); and (f) $t_h$ = 45 min ($Au_{21}Cu_{79}$). Feeding Cu/Au molar ratio: 8.5 (a, b, c, e), 4.0 (d), and 12.8 (f). (a–f: $T$ = 156 °C).
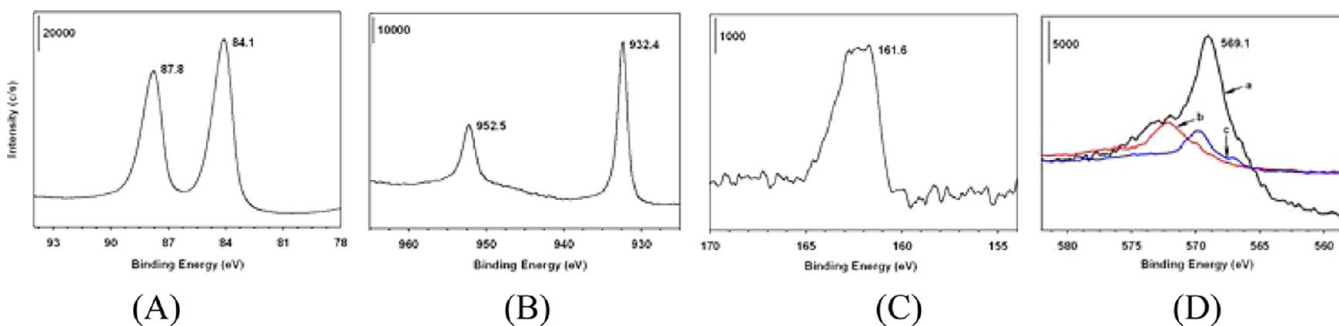


**Figure 6.** XPS spectra. (A−C) a sample of $Au_{66}Cu_{34}$ nanoparticles obtained by a thermal treatment at $T$ = 156 °C for 3 h. (A) Au 4f, (B) Cu 2p, and (C) S 2p regions (Au/Cu atomic ratio found by XPS, 48:52). (D) AES spectra in the Cu LMM region (the main peak position at 569.1 eV) for samples of $Au_{66}Cu_{34}$ (a, cubes, black), $Cu_2S$ (b, red) and Cu-DT (c, blue) nanoparticles.

for bulk Au (0.408 nm) and bulk Cu (0.361 nm), this lattice value seemed to be in line with Au, which is, however, diminished by the broad feature of the Bragg peaks. The AuCu nanoparticles were found to show a narrowed peak width after being thermally processed, displaying a lattice constant of 0.407 nm, falling in between those for bulk Au (0.408 nm) and bulk Cu (0.361 nm). The precise determination of the lattice parameter that confirms the alloying characteristic will be discussed in the later sections where synchrotron X-ray and high energy XRD are used for the characterization.

**2. Nanoscale Alloying via Thermal Evolution of Mixed Au and Cu Nanoparticles.** *Morphological Evolution.* The solid-like behavior of nanoparticles can be understood by comparing the theoretical melting curves for Au, Cu, Ag, and Pt as a function of particle sizes ($r$-radius)[1,23] (Supporting Information Figure S2 and Table S1). For nanoparticles smaller than 2 nm in diameter, the theoretical melting temperatures ($T_r$), are much lower than their bulk ones, exhibiting $T_r$ (Cu) < (Au) ∼ (Ag) ≪ (Pt). The surface melting temperature could be significantly lower at $r$ < 2 nm than the theoretical ones,[23] as found from earlier studies of the thermal evolution of Au nanoparticles[1,2] and thiolate-capped Cu nanoclusters to $Cu_2S$ nanodiscs.[3] Results are shown to demonstrate how structural evolution can be achieved at or near such a temperature.

Figure 4 shows a set of TEM micrographs for Au (Figure 4A, 2.0 ± 0.7 nm), Cu nanoparticles (Figure 4B, ∼0.5 nm) capped with a DT monolayer, and Au nanoclusters capped by

octadecanethiol (∼1 nm). The size characteristics of the as-synthesized thiolate-capped copper nanoclusters were examined by a combination of SAXS and WAXS experiments (insert in Figure 4B) and Maldi-TOF mass analysis (Supporting Information Figure S3). In the SAXS and WAXS data, a peak observed at $q$ = 13.4 nm$^{-1}$ was used to calculate the interparticle distance ($d$ = $2\pi/q$, where $d$ is the interparticle core distance) yielding an intercore distance of 0.5 nm (Figure 4B). The average particle size was estimated to be close to or less than 0.5 nm. The Maldi-TOF mass data suggest the presence of $Cu_{5-7}$ clusters such as $Cu_5(SR)_4$, $Cu_5(SR)_5$, $Cu_6(SH)_3SR$, $Cu_7(SH)_4SR$, and $Cu_7(SH)_2(SR)_2$.

AuCu nanocubes were obtained by carefully controlling the temperature and Cu/Au molar ratio. For example, $Au_{66}Cu_{34}$ nanocubes were obtained by heating a binary solution of Cu nanoclusters and Au nanoparticles using a Cu/Au molar ratio of ∼8 at $T$ = 156 °C (Figure 4D−F). At a lower temperature (e.g., 150 °C), various shapes (spheres, triangles, cubes, hexagons, etc) are evident. At a higher temperature (e.g., 172 °C), the particles become largely aggregated. Note that the products of the thermal processing were subjected to cleaning cycles via suspension in ethanol and acetone, and centrifuged at least four times to ensure a complete removal of the solvent and possible byproducts.

By HR-TEM analysis (Figure 4G−I), the average (100) interatomic layer distance of the nanocubes (Figure 4I) is found to be 0.194 nm, which is close to the fcc-type interatomic layer distance ∼0.187 nm of the (100) planes for AuCu nanocubes
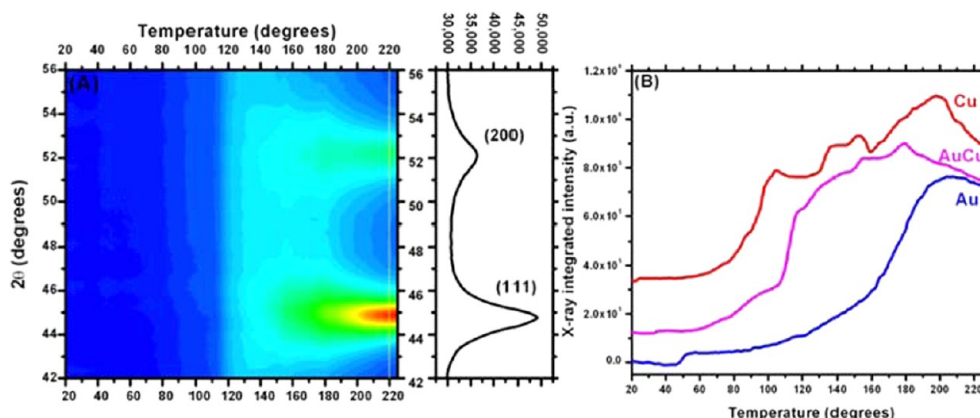
**Figure 7.** In situ real-time synchrotron XRD. (A) Map showing evolution during uniform ramping from 25 to 225 °C for binary Au nanoparticles (2 nm) and Cu nanoclusters with a Cu/Au molar ratio of 8.5 cast on a Si surface and a snapshot of XRD pattern at 220 °C; (B) comparison of temperature evolution of (111)-intensity for Au, Cu, and binary (1:1) Au and Cu. (X-ray energy: 6.9 keV).

prepared by a different method.[10] Both the lattice fringes and the fast-Fourier transform (FFT) pattern reveal (200) interatomic planes separated at distances of 0.187 and 0.193 nm, respectively. The slight difference of lattice constants computed from the HR-TEM data in a perpendicular direction is indicative of a possible tetragonal distortion that is found in ordered AuCu alloys .

The size and shape of the nanoparticles were also found to depend on the heating time and Au/Cu mixing ratio. TEM data for samples obtained by the mixing of Au and Cu (1:1 ratio) and thermally treated for different time lengths are shown in Figure 5. For thermal processing time of 1.5 h, a bimodal size distribution is observed, including nanocubes (~3.5 nm) and smaller-sized nanoparticles (<2 nm). For longer processing time (>4.5 h), the particles appeared to be predominantly spherical (~4.5 nm). For a Cu/Au mixing molar ratio <8 (Figure 6D−F) ~10% nanocubes and ~90% nanopheres (~5 nm) were observed, with a predominance of larger Au nanoparticles,[1,2] while~30% nanocubes (~6 nm) and ~55% nanodiscs (~12 nm) were observed for a Cu/Au molar ratio >8, suggestive of a competitive growth of AuCu alloy and $Cu_2S$ particles due to the faster evolution of Cu nanoclusters.[3]

Note that a thermal evolution of Au nanoparticles leads to larger sizes[1] and that for Cu nanoparticles leads to $Cu_2S$.[3] To substantiate the important roles of nanoscale melting and cross reactivity in the alloying process, different binary combinations such as Cu + Pt and Cu + Ag at similar processing temperatures and mixing ratios were also examined (Supporting Information Figure S4). For binary Cu and Pt nanoparticles, the morphology of Pt was found to remain, whereas Cu nanoparticles evolved into $Cu_2S$ nanodiscs. The difference of the melting temperatures between Pt and Cu is too large for the two to coexist in partial melt states and coalesce into an alloy at this temperature. For binary Cu and Ag, a size growth was observed, consistent with the small difference of their melting points, which allows coalescence into alloy nanoparticles. By eating a binary solution of Au nanoparticles and $Cu^{2+}$ in the absence or presence of reducing agents, larger-sized (9 nm) Au nanoparticles were obtained in the former case, and a mixture of larger-sized (9 nm) Au nanoparticles and $Cu_2S$ nanorods/ disks were observed in the latter case, showing no indication of the formation of the alloy, demonstrating the important role of the nanoparticle precursors in the formation of the alloy nanocubes.

*Structural Evolution.* The structural evolution was examined using XPS and in situ wide angle synchrotron XRD techniques. The XPS analysis provides information for assessing the relative surface composition. For a feeding Cu/Au molar ratio of 8.5 at 156 °C for 3 h, the dominant shape of the resulting nanoparticles was a thiolate-capped nanocube (~3.6 nm) with a bimetallic composition $Au_{66}Cu_{34}$, as determined by ICP analysis and substantiated by XPS and surface plasmon resonance characterizations (Figure 6). XPS analysis of the AuCu alloy nanoparticles (Figure 6) showed doublet peaks characteristic of Cu (2p) (932.5 eV for Cu ($2p_{3/2}$) and 952.5 eV for Cu ($2p_{1/2}$)), consistent with literature values.[28,29] In the S (2p) region, the doublet peak is detected at 163.5 and 162.3 eV for $2p_{3/2}$ and $2p_{1/2}$, respectively. The binding energy values for Cu ($2p_{1/2}$) and Au (4f) were found to be in good agreement with those reported previously.[12] In the Cu LMM region, the main peak position (569.1 eV) (Figure 6D) indicates that copper is in the Cu (0) state for the alloy nanocubes. The higher-energy shoulder indicates the presence of $Cu^+$ peak from $Cu_2S$. The S 2p and Au 4f peaks are consistent with the presence of thiolate-capping molecules and Au in the nanoparticles. Note that the nanoalloy character was also supported by a surface plasmon resonance band at ~560 nm, characteristic of AuCu alloys with sizes larger than 3 nm.[30]

An analysis of in-house XRD patterns (Supporting Information Figure S5A) shows a high intensity ratio of (200) vs (111) peak for the nanocubes, which is consistent with a preferred orientation of the nanocubes on the substrate. For the case of a bimodal distribution (Figure 5a), the XRD pattern is basically identical to that for an alloyed AuCu nanoparticle samples prepared by other methods.[10,30] The solution-phase evolved AuCu alloy nanocubes deposited on a Si-substrate were further examined by in situ wide angle XRD technique[31] (Supporting Information Figure S5B). For AuCu nanocubes, the ratio of peak intensities and widths for (111) and (200) are consistent with a cubic shape, in contrast to the (111)/(200) ratio of ~2 for spherical particles. After annealing at 260 °C, the peak ratio changes to >2, similar to that observed with spherical particles. The lattice constant computed from the positions of the many Bragg peaks decrease from 4.05 Å to 3.92 Å indicating an additional diffusion of Cu in Au and a further evolution into spherical shapes likely due to particles sintering as evidenced by the size increase to about 6.5 nm in diameter.
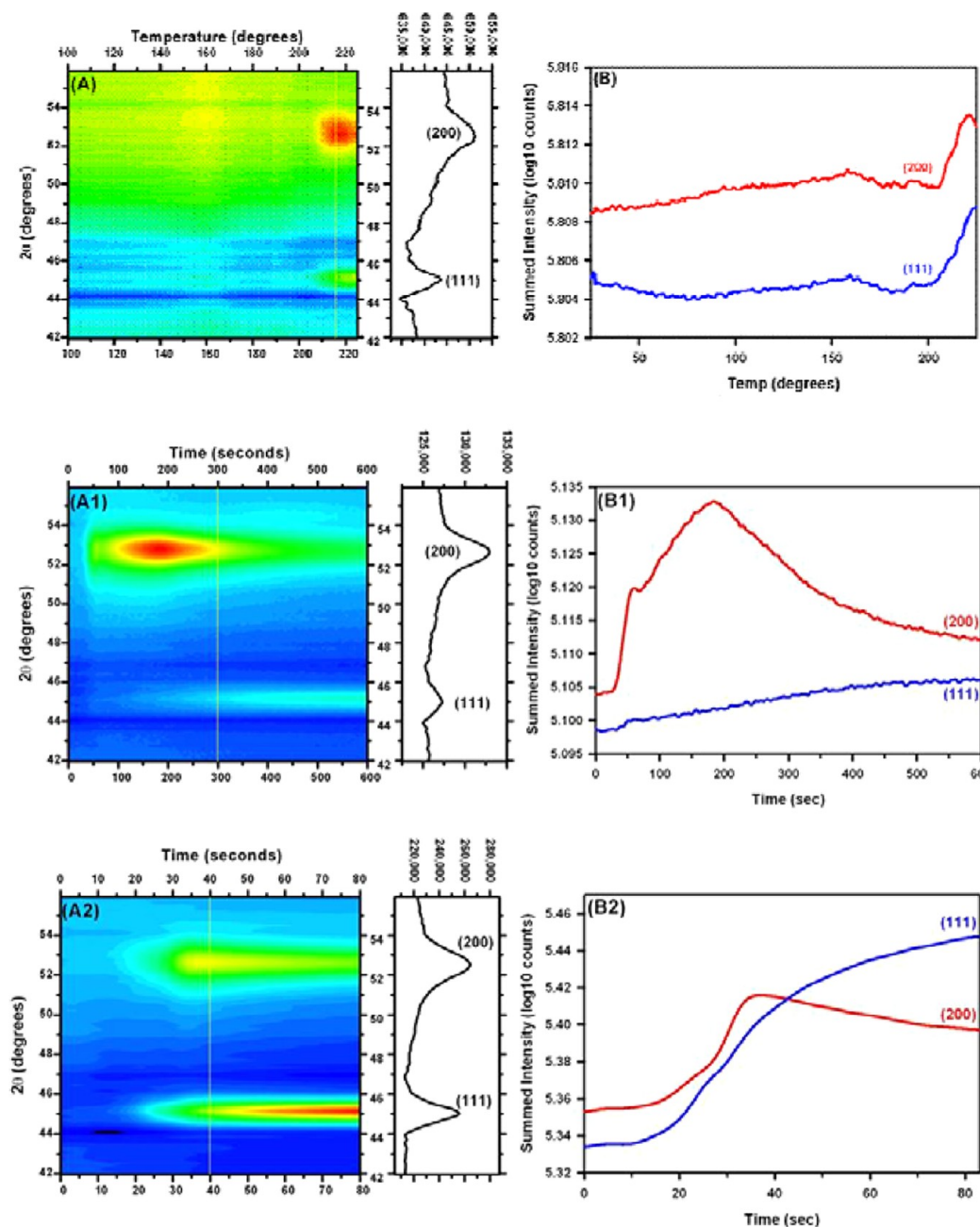
**Figure 8.** In situ real-time synchrotron XRD for the temperature evolution of a binary solution of Au nanoclusters (<1 nm) and Cu nanoclusters with a Cu/Au molar ratio of 8.5 (A, B); In situ real-time synchrotron XRD for the time evolution of binary Au (<1 nm) and Cu nanoclusters with a Cu/Au molar ratio of 8.5 at 190 °C (A1, B1) and at 210 °C (A2, B2), including a map showing evolution for (111) and (200), and a snapshot of XRD pattern at 300 s (A1, B1) and 40 s (A2, B2).

Figure 7A, B shows the behavior of the wide angle XRD patterns during uniform heating from 25 to 225 °C of a binary solution of 2-nm Au and 0.5-nm Cu cast on a planar Si substrate. The temperature evolution of the binary sample is compared with the evolution of unary Cu and unary Au nanoparticle samples in Figure 7B. Due to the smaller size and lower melting point, the Cu particles start to aggregate immediately after heating above 60 °C. In sharp contrast, the Au nanoparticles restructure significantly only above 140 °C. In terms of the "half-way" temperature for the increase of the integrated intensity, the temperature for Cu + Au (~115 °C) falls in between those for Au (~160 °C) and Cu (~90 °C). Since this temperature is relatively low compared to the melting

temperature of 2 nm Au nanoparticles, the restructuring process likely involves solid-phase sintering and recrystallization. The physical mixture exhibits an intermediate behavior, but it is clear that the particles restructure at considerably lower temperatures than pure Au nanoparticles, indicating a significant effect of the Cu nanoparticles.

Below 100 °C, the increase of the integrated Bragg peak intensity can only be attributed to a coalescence of the Cu nanoparticles. Above 100 °C, the rapid growth is likely due to Cu-mediated interaction between the Au nanoparticles resulting in the formation of an incompletely alloyed phase, as indicated by the lattice constant values. We believe that the alloying process occurs through a coalescence and mixing of a
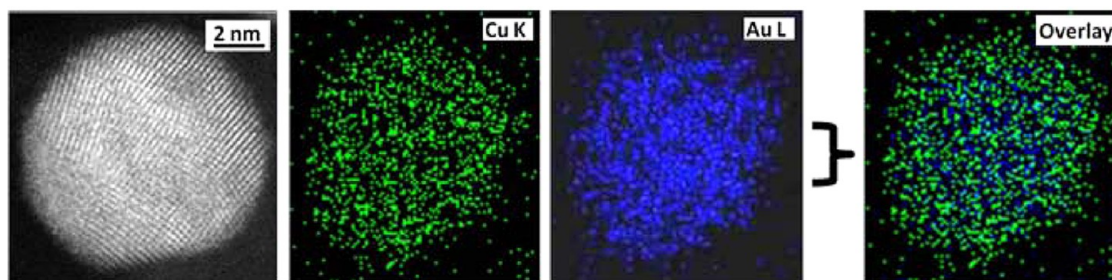
**Figure 9.** High-angle annular dark-field scanning TEM (HAADF-STEM) image for morphological imaging (the most left image) and EDS images for elemental mapping of a sample of $Au_{40}Cu_{60}$/C.

disordered/melted Au surface layer with liquid Cu droplets. Once the nanoparticle becomes large enough (~4 nm) to be more stable in the crystalline phase, they solidify in the fcc-type structure. It is thus possible that the excess energy resulting from the negative heat of formation for alloying as well as from the decreased surface energy leads to an increase of the internal temperature, which likely facilitates the reshaping of the nanoparticle into nanocubes.

The detailed structural evolution was further probed for a binary system consisting of Cu and Au nanoclusters (<1 nm) by real-time wide angle XRD using a synchrotron source (Figure 8). Since both particles were small (<1 nm), we were able to capture the relative changes of the strongest (111) and (200) Bragg peaks only. During a uniform temperature ramping from 25 to 225 °C (Figure 8A), both peaks show a transient maximum at about 160 °C which may be associated with the formation and dissolution of $Cu_2S$ nanodiscs. In Figure 8A,B, a map of the evolution of (111) and (200) Bragg peaks, and a snapshot of XRD pattern at 215 °C, are shown.

The structural evolution of the nanoparticles was further probed for a binary system consisting of Cu and Au nanoclusters (<1 nm) by real-time wide angle XRD. Since both nanoclusters were very small (<1 nm), we were able to capture the relative changes of the strongest (111) and (200) Bragg peaks only. During a uniform temperature ramping from 25 to 225 °C, both peaks show a transient maximum at around 160 °C, which we again associate with the formation and dissolution of $Cu_2S$ nanodiscs. Further temperature increase leads to a sharp increase in the intensity of both peaks at 210 °C. A larger (200)/(111) than the observed in Figure 8A1, B2 intensity ratio suggests the formation of (200) preferentially oriented nanoparticles, most likely with the shape of nanocubes. Patterns taken at 190 °C (Figure 8A1, B1) and 210 °C (Figure 8A2, B2), were used to assess the relative changes of the (200) and (111) peaks. At 190 °C (Figure 8B), the (200) Bragg peak showed a sharp rise before starting a slow decay after 200 s, in contrast to the persistent slow rise of the (111) Bragg peak. The snapshot XRD pattern at ~300 s clearly showed an increased intensity ratio of (200) vs (111) peaks, a piece of evidence supporting the formation of alloy nanocubes at the initial stage of the evolution. At 210 °C, the XRD pattern shows a similar initial behavior (with a dominant (200) peak shown in the snapshot at 40 s), but upon further annealing the pattern quickly returns to the typical (200)/(111) ratios indicative of spherical particles. The internal energy possibly resulting from the negative heat of formation between Au and Cu (alloying) could lead to a rise of the particles internal temperature, thus creating a condition for alloying and reshaping from a cube-shaped intermediate toward an fcc-type alloy nanocube via further partial melting–resolidification.

The morphology of small copper nanoparticles (smaller than about 4 nm) is often of an icosahedral or decahedral type that usually occurs with noncrystalline materials. On the other hand, the morphology of copper particles larger than 4 nm can be icosahedral, decahedral, or of a fcc crystalline type.[32] It is also known that the situation with gold nanoparticles is rather similar.[33] The evolution from icosahedral or decahedral to fcc is unlikely to occur through a direct solid–solid transition; rather, it is likely to go through a solid–liquid coexistence and a phase transition.[7] In this case, the small particles can become superheated.[34] Based on the experimentally observed fcc-type cubic shape for the evolved AuCu alloy nanoparticles and the in situ XRD data showing a gradual increase of the fcc-type atomic ordering, it is possible that a stable solid–liquid phase coexistence takes place involving surface melting.[7] The difference in the speed of growth of the different nanoparticles is likely caused by the varying free energy of their facets and the varying binding strength of the thiolate capping molecules. It is known that thiolates adsorb more strongly to the 100 facets of the cuboctohedron, and so, the 111 facets grow at a faster rate than the 100 faces leading to the formation of cube-shaped particles instead of spherical shaped ones.

Surface reconstruction has been reported for Cu and Au nanoparticles, and energetic surface reconstruction phenomena were observed on bimetallic AuCu nanoparticles with truncated 5-fold edges, resulting in (100) facets and decahedral-type morphologies.[35] Studies of phase conformations and thermal behavior of AuCu binary clusters by classical molecular dynamics simulations showed that the cluster size, the concentration in the alloy, and the annealing temperature have a dominant effect on this morphology reconstruction process.[36] For example, when the starting morphology is of a cuboctahedral type, by changing the concentration of copper from 50 to 10%, an optimum stability of an icosahedral-type morphology is found at a bimetallic concentration of gold 75% and copper 25%, in fair agreement with experimental reports.

Taken together, the evolution of the morphology of Cu or Au nanoparticles (<4 nm) from icosahedral or decahedral noncrystalline structures[32,33] to fcc-type structures likely includes both a solid–liquid coexistence and a phase transition stage.[7,32] The kinetic difference in which the thiolates adsorb strongly to 100 faces of cuboctohedron and the 111 faces grow faster than 100 faces, which is also consistent with the energetic surface reconstruction for bimetallic AuCu nanoparticles. The "molecule-solid" duality is further reflected by the fact that AuCu nanoalloy is the preferred reaction product over the unary evolution of Cu to $Cu_2S$ nanodiscs[3] and Au to Au nanoparticles.[2] This conclusion is supported by the trend of known interatomic interaction energies Au–Au (3.81 eV) > Cu–Au (3.75–3.64 eV) > Cu–Cu (3.49 eV),[37] and the bulk
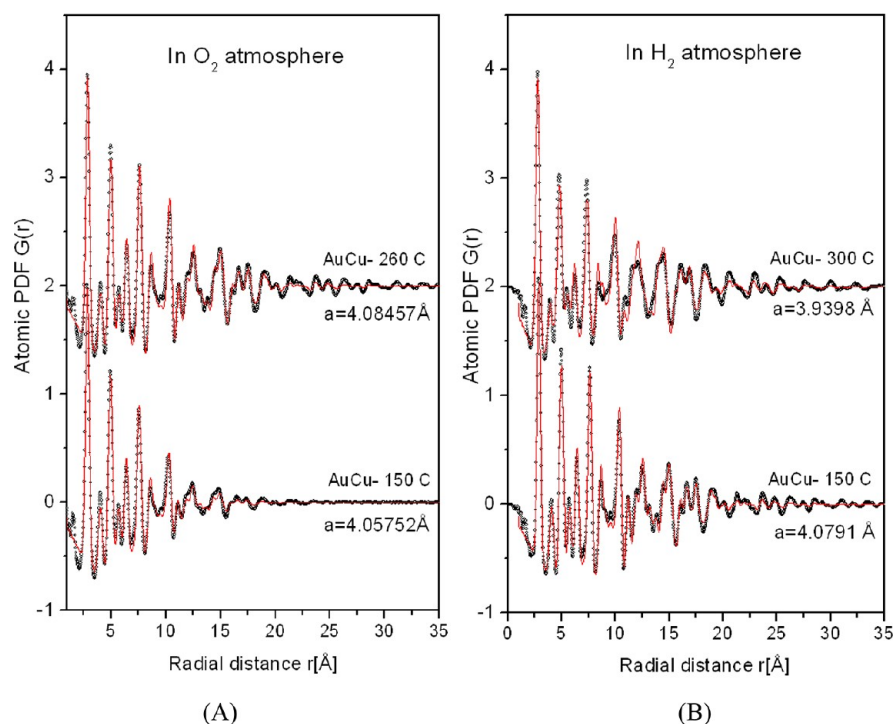
**Figure 10.** Atomic PDFs for $Au_{51}Cu_{49}/C$ nanoalloys supported on carbon obtained from in situ HE-XRD data collected under controlled temperature and oxidative ($O_2$)/reductive ($H_2$) atmosphere. Experimental data, symbols; computed data, red solid line. The computed data feature fits based on an fcc-type structure. The catalyst was subjected sequentially to two different treatment conditions: (A) under 10 vol % $O_2$, first heating to 150 °C (bottom curve) and then heating to 260 °C (top curve); (B) under 5 vol % $H_2$, first heating to 150 °C (bottom curve) and then heating to 300 °C (top curve).
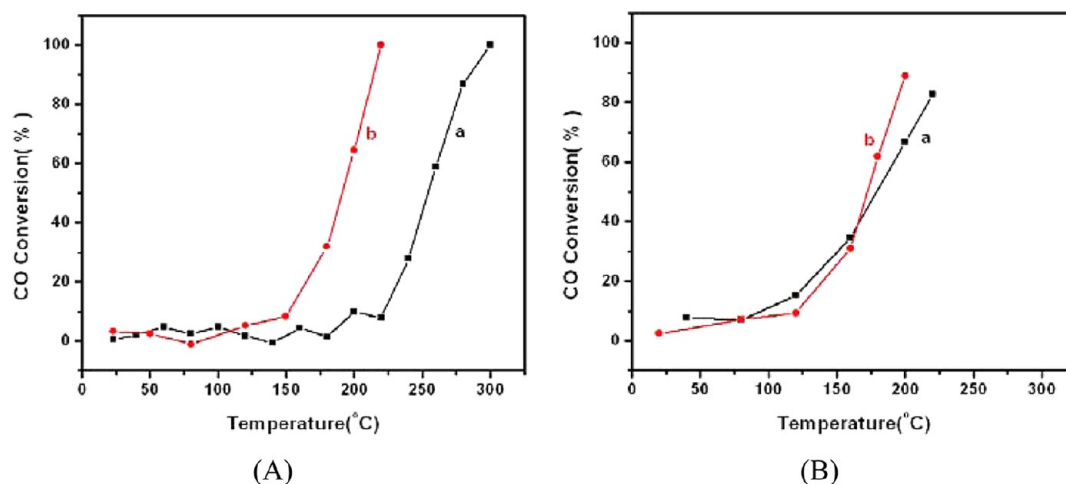


**Figure 11.** CO conversion as a function of the reaction temperature for samples of $Au_{51}Cu_{49}/C$ catalyst (A) and $Au_{11}Cu_{89}/C$ (B): (a, black) activity after oxidative treatment (20 vol % $O_2$ 260 °C, 1 h), and (b, red) activity of the post-a catalyst after reductive treatment (15 vol % $H_2$, 400 °C, 1 h).

melting temperature Cu (1084 °C) > Au (1064 °C) > CuAu alloy (947 °C)[38] (Supporting Information Figure S2).

**3. Structures of Supported AuCu Catalysts and Catalytic Activity.** *Morphology and Composition of the Bimetallic Nanoalloy Catalysts.* AuCu nanoparticles were supported on carbon, and subjected to thermal treatments under 260 °C (in 15% $O_2$) and then under 400 °C (15% $H_2$). The average sizes of the nanoparticles are 4.5 ± 1.3 nm for $Au_{38}Cu_{62}/C$ and 4.2 ± 0.7 nm for $Au_{11}Cu_{89}/C$. The XRD patterns reveal an fcc-type of alloy structure with an a lattice constant of 0.410 nm falling in between that for bulk Au (0.408 nm) and bulk Cu (0.361 nm). Figure 9 shows a set of images

obtained from high-angle annular dark-field scanning TEM (HAADF-STEM) imaging for morphology characterization and energy dispersive X-ray spectroscopy (EDS) for elemental mapping for a sample of $Au_{40}Cu_{60}/C$ catalyst. The HAADF images reveal high crystallinity and multiple facets. The detected Cu and Au concentration in the nanoparticles is $Au_{42}Cu_{58}$ in an excellent agreement with composition determined by ICP. The overlap of the Cu and Au metal distribution shows a good degree of alloying across the entire nanoparticle. Interestingly, the overlapped image seems to suggest a slightly higher concentration of Cu along the outer

layer of the alloy particle, which is quite consistent with the XPS analysis results described earlier.

*Atomic-Scale Structural Changes of the Bimetallic Nanoalloy Catalysts.* The atomic-scale structural changes of the nanoalloy catalysts under different thermochemical conditions were examined by HE-XRD/PDFs analysis. Figure 10 shows a set of atomic PDFs extracted from in situ high-energy synchrotron XRD data for a sample of $Au_{51}Cu_{49}/C$ catalyst treated under oxidative ($O_2$) and reductive ($H_2$) conditions at two temperatures. The fits to the PDFs feature an fcc-type structure. For the initial catalyst at room temperature, the refined lattice parameter was 4.0458 Å. Under $O_2$, the lattice parameter is seen to increase with temperature from $a = 4.0575$ Å at 150 °C to $a = 4.0846$ Å at 260 °C. The lattice parameter remains "increased" at $a = 4.0706$ Å after the sample is cooled to room temperature. There are no detectable signatures of a second phase indicating a very good degree of alloying. Under $H_2$, the lattice parameter is found first to increase, due to the usual thermal expansion, and then to decrease with increasing temperature from $a = 4.0791$ Å at 150 °C to $a = 3.9398$ Å at 300 °C. The lattice parameter remains "decreased" after the sample has been cooled to room temperature ($a = 3.9225$ Å). There are no detectable signatures of a second phase again indicating a very good degree of alloying.

*Catalytic Activities for CO Oxidation.* The question of how the bimetallic sites of the AuCu nanoparticles function catalytically was probed by determining the CO oxidation activity. Figure 11A shows a typical set of CO conversion data as a function of the reaction temperature for $Au_{51}Cu_{49}/C$ catalyst under CO + $O_2$ atmosphere. The initial activity of the catalyst, after it was treated for 1 h in $O_2$ was quite low, as indicated by the moderate rise of activity (~10%) near 200 °C (a). However, upon a reduction treatment of the catalyst under 15 vol % $H_2$ (400 °C for 1 h), the catalytic activity was significantly increased, as evidenced by an activity of ~65% at 200 °C and the rise in temperature near 120 °C (Figure 11b). This finding indicates that the nanoalloy is more active than the as-prepared catalyst that is possibly partially oxidized on the surface.

The role of copper in the nanoalloy's activity is further probed for a catalyst with a higer percentage of Cu in the nanoparticles ($Au_{11}Cu_{89}/C$ catalyst). In this case, the initial activity was clearly higher than the $Au_{51}Cu_{49}/C$ catalyst, as evidenced by the activity of ~90% at 200 °C and the onset of activity near room temperature. Surprisingly, the activity showed a much smaller degree of dependence on the oxidative and reductive treatments. At 150 °C, the oxidation-treated and the reduction-treated catalysts showed quite similar activities (~30% vs 25%). At 200 °C, the activity of the reduction-treated catalyst (~90%) was slightly higher than that of the oxidation-treated catalyst (~65%). This finding indicates that a Cu-dominant nanoalloy functions not only as an active but also relatively stable catalyst under the thermochemical and catalytic reaction conditions. It is possible that copper oxide may have partially contributed to the catalytic activity. However, in order to make a meaningful comparison of the catalytic activities between $CuO_x$ and AuCu, it is necessary to have similar particle sizes and controlled surface properties and oxidation degrees, which is part of our efforts in future investigations.

The catalyst was also supported on $SiO_2$, which is also an oxygen-inactive support but can sustain a higher thermal treatment temperature than carbon support, to examine the effect of a "deep oxidation" (i.e., at a higher temperature of the

thermochemical treatment under $O_2$) on the activity. In Figure 12, a typical set of CO conversion data is shown for a catalyst
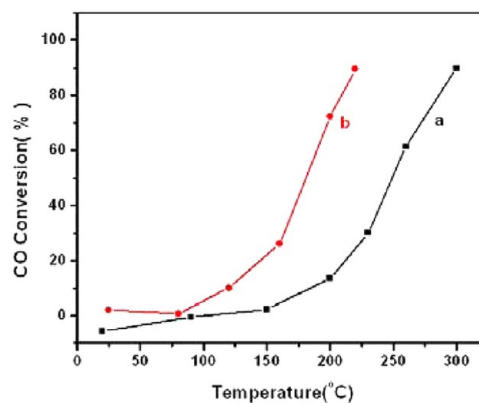


**Figure 12.** CO conversion as a function of the reaction temperature for a sample of $Au_7Cu_{93}/SiO_2$ catalyst: (a) activity after an oxidative treatment (20 vol % $O_2$ 500 °C, 1 h), and (b) activity of the catalyst after a reductive treatment (15 vol % $H_2$, 400 °C, 1 h).

sample with a similarly high percentage of copper in the AuCu nanoparticles supported on silica. The catalytic activities were compared between initial treatment at 500 °C under $O_2$ and after treatment at 400 °C under $H_2$. In this case, the characteristics in catalytic activity are apparently not the same as those shown for $Au_{11}Cu_{89}/C$ catalyst in Figure 11B. Rather, the activity changes are quite similar to those observed for $Au_{51}Cu_{49}/C$ catalyst (see Figure 11A) with subtle differences in terms of activity onset temperature. The onset temperature is slightly lower than that for the $Au_{51}Cu_{49}/C$ catalyst. This finding suggests that the "deep oxidation" treatment of the nanoalloy on silica, while affecting the catalytic activity to a certain degree, still leads to reduced activity in comparison with that of the reduced one.

The finding is remarkable considering the recent results reported for AuCu on $TiO_2$ prepared by different methods.[18a,b] For silica supported AuCu nanoparticles (with an unspecified bimetallic composition),[18a] an oxidation treatment at 500 °C was found to produce a segregation of Au and CuO and show 100% CO conversion at temperature slightly above 0 °C. The catalyst deactivates when it is reduced in $H_2$ at 300 °C. A similar trend was also observed for a Au–Cu/SBA-15 catalyst ($Au_xCu_{1-x}$ ($0.95 > x > 0.8$)) for preferential oxidation of CO in $H_2$-rich gas,[18b] in which the oxidation of the catalyst was shown to increase activity due to phase segregation of Au from $CuO_x$, which deactivated upon its reduction to an alloy state. We believe that the different catalytic characteristics reflect the difference in the degree of alloying and the structural stability of the catalyst. In the reported AuCu systems, the oxidation leads to a phase segregation of the copper oxide species so that copper oxide serves as an oxygen-active support to Au. For our AuCu system, the oxidation does not lead to a phase segregation, rather the formation of surface oxygenated Cu species. This assessment is supported by the in situ XRD/PDFs analysis results. Based on our recent study of ternary nanoalloys of Pt with different transition base metals,[39−41] it is believed that the oxygenated metal species in the nanoalloy provide oxygen storage and release capacity, creating bifunctional surface sites where the Pt-site activates CO whereas the oxygenated base metal activates oxygen. The copper species in our AuCu nanoalloys provide activated $O^{\delta-}$ species in the

**Scheme 2. Illustration of the Proposed Catalytic CO Reaction on a Supported AuCu Catalyst in Either Reduced Nanoalloy (A) or Oxidized Nanoalloy (B) States, where Cu Provides Sites for the Surface Oxygenating Sites Involving $O^{2-}$ and $O^{\delta-}$ Species or Oxidized and Phase-Segregated State (i.e., Au Nanoparticles Supported on $CuO_x$) (C)**[a]
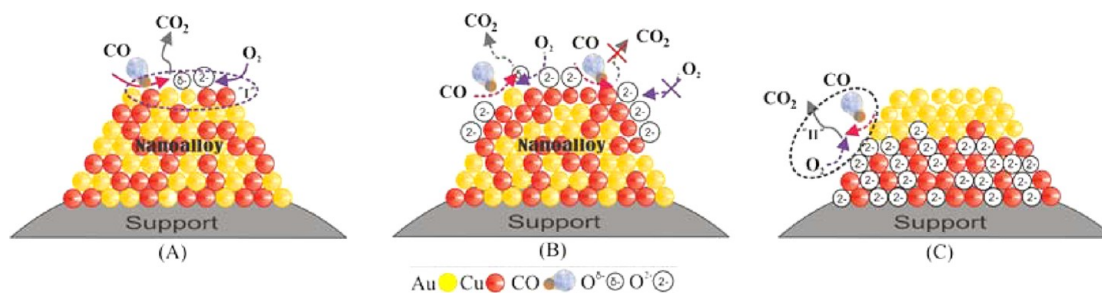


[a]"I" site for $O_2$ activation exists largely on reduced nanoalloy surface (case A), not on the oxidized one where the surface is completely blocked by the oxide species ($O^{2-}$, case B). "II" sites for $O_2$ activation exist for case C.

oxidation reaction of carbon monoxide, which operates effectively under the condition of <90% Cu in AuCu alloy (Case A in Scheme 2). This type of $O_2$ activation site exists largely on a reduced nanoalloy surface. Upon oxidation, the surface is completely blocked by oxide species (case B in Scheme 2), which explains the low catalytic activity of the oxidized $Au_{51}Cu_{49}/C$ catalyst. When Cu is >90%, there are two possible scenarios. The first scenario is that alloy does not exist on the oxidized nanoparticle surface (case B in Scheme 2). Second, the oxygenated copper species undergo a phase segregation to produce $CuO_x$ supported Au nanoparticles (case C in Scheme 2) in which certain Au sites on the surface are fully surrounded by CuO. In the last case, the well-known particle-support premier site would be operative for oxygen activation. These two scenarios could explain the relatively comparable activities between the reduced and oxidized $Au_{11}Cu_{89}/C$ catalysts. How the catalytic activity correlates with the bimetallic composition is yet to be further investigated.

## CONCLUSION

In conclusion, effective strategies have been demonstrated for controlling the formation of AuCu nanoalloys and their atomic-scale structure under the controlled thermochemical conditions for exploiting the bifunctional catalytic properties. Two pathways have been explored for the formation of AuCu nanoalloys, including wet chemical synthesis from mixed Au- and Cu-precursor molecules, and nanoscale alloying via thermal evolution of mixed Au- and Cu-precursor nanoparticles. For the evolution of the mixed precursor nanoparticles, nanoscale alloying and reshaping toward nanoparticles with a nanocube morphology via a partial melting-resolidification mechanism was revealed by synchrotron X-ray-based in situ real-time XRD characterization. For the carbon or silica supported AuCu catalysts an intriguing lattice "expansion–shrinking" phenomenon of the nanoalloys depending on whether the thermal treatment condition is oxidative or reductive is revealed by in situ HE-XRD/PDFs analysis. This type of structural change and stability is found to play an important role in determining the bifunctional catalytic activity for CO oxidation. The oxygenated copper species in the nanoalloy provides oxygen storage and release capacity for the catalysts with <90% Cu in AuCu alloy, where $O_2$ activation occurs on the reduced nanoalloy surface. The catalyst deactivates upon treatment under oxidative atmosphere. The sharp contrast of the observed catalytic activity changes in response to oxidative–reductive treatment from those reported previously for $AuCu/SiO_2$ prepared

differently demonstrates the importance of the nanoscale alloying and structural/chemical ordering of the nanoalloys in the catalytic properties, which are achieved by the effective nanoscale alloying strategies described in the report. We note that a direct comparison of the data with the literature data cannot be made at this point because of the very different methods used for the preparation of the AuCu systems and the different bimetallic composition in the catalysts. To compare the catalytic activities of our nanoalloys with the literature work (AuCu of either Au-rich (>80%) or unspecified bimetallic composition[18]), it is necessary to prepare both the nanoalloys and the phase-segregated nanostructures from the same preparation condition with the same bimetallic composition, which is part of our ongoing work.

## ASSOCIATED CONTENT

**Ⓢ Supporting Information**

Additional TEM, XRD, and Maldi-TOF data. This material is available free of charge via the Internet at http://pubs.acs.org.

## AUTHOR INFORMATION

**Corresponding Author**
*E-mail: cjzhong@binghamton.edu.

**Present Address**
#School of Materials Science, Japan Advanced Institute of Science and Technology, 1-1 Asahidai, Nomi, 923-1292 Ishikawa, Japan

**Notes**
The authors declare no competing financial interest.

## ■ REFERENCES

(1) (a) Maye, M. M.; Zheng, W. X.; Leibowitz, F. L.; Ly, N. K.; Zhong, C. J. *Langmuir* **2000**, *16*, 490. (b) Schadt, M. J.; Cheung, W.; Luo, J.; Zhong, C. J. *Chem. Mater.* **2006**, *18*, 5147.

(2) (a) Luo, J.; Maye, M. M.; Petkov, V.; Kariuki, N. N.; Wang, L.; Njoki, P.; Mott, D.; Lin, Y.; Zhong, C. J. *Chem. Mater.* **2005**, *17*, 3086. (b) Wanjala, B. N.; Luo, J.; Fang, B.; Mott, D.; Zhong, C. J. *J. Mater. Chem.* **2011**, *21*, 4012. (c) Maye, M. M.; Kariuki, N. N..; Luo, J.; Han, L.; Njoki, P.; Wang, L.; Lin, Y.; Naslund, H. R.; Zhong, C. J. *Gold Bull.* **2004**, *37*, 217.

(3) (a) Mott, D.; Yin, J.; Engelhard, M.; Loukrakpam, R.; Chang, P. G.; Bae, I.-T.; Das, N. C.; Wang, C.; Luo, J.; Zhong, C. J. *Chem. Mater.* **2010**, *22*, 261. (b) Park, H. Y.; Schadt, M. J.; Wang, L.; Lim, I-I. S.; Njoki, P. N.; Kim, S. H.; Jang, M.-Y.; Luo, J.; Zhong, C. J. *Langmuir* **2007**, *23*, 9050.

(4) Yin, J.; Hu, P.; Wanjala, B.; Malis, O.; Zhong, C. J. *Chem. Commun.* **2011**, *47*, 9885.

(5) Parker, J. F.; Fields-Zinna, C. A.; Murray, R. W. *Acc. Chem. Res.* **2010**, *43*, 1289.

(6) Baletto, F.; Ferrando, R. *Rev. Mod. Phys.* **2005**, *77*, 371.

(7) Yeshchenko, O. A.; Dmitruk, I. M.; Alexeenko, A. A.; Dmytruk, A. M. *Phys. Rev. B* **2007**, *75*, 085434.

(8) Sra, A. K.; Schaak, R. E. *J. Am. Chem. Soc.* **2004**, *126*, 6667.

(9) Chen, W.; Yu, R.; Li, L.; Li, Y. *Angew. Chem., Int. Ed.* **2010**, *49*, 2917.

(10) Liu, Y.; Walker, A. R. H. *Angew. Chem., Int. Ed.* **2010**, *49*, 6781.

(11) Henkel, A.; Jakab, A.; Brunklaus, G.; Carsten, S. *J. Phys. Chem. C* **2009**, *113*, 2200.

(12) Llorca, J.; Domíngueza, M.; Ledesmaa, C.; Chimentãob, R. J.; Medinab, F.; Sueirasb, J.; Angurellc, I.; Secoc, M.; Rossellc, O. *J. Catal.* **2008**, *258*, 187.

(13) Bracey, C. L.; Ellis, P. R.; Hutchings, G. J. *Chem. Soc. Rev.* **2009**, *38*, 2231.

(14) Liu, X.; Wang, A.; Wang, X.; Mou, C. Y.; Zhang, T. *Chem Comm.* **2008**, *27*, 3187.

(15) Pina, C. D.; Falletta, E.; Rossi, M. *J. Catal.* **2008**, *260*, 384.

(16) Gluhoi, A. C.; Bogdanchikova, N.; Nieuwenhuys, B. E. *Catal. Today* **2006**, *113*, 178.

(17) Chang, F. W.; Ou, T. C.; Roselin, L. S.; Chen, W.-S.; Lai, S.-C.; Wu, H.-M. *J. Mol. Catal. A: Chem.* **2009**, *313*, 55.

(18) (a) Bauer, J. C.; Mullins, D.; Li, M.; Wu, Z.; Payzant, E. A.; Overbury, S. H.; Dai, S. *Phys. Chem. Chem. Phys.* **2011**, *13*, 2571. (b) Li, X.; Fang, S.; Teo, J.; Foo, Y. L.; Borgna, A.; Lin, M.; Zhong, Z. *ACS Catal.* **2012**, *2*, 360.

(19) (a) Wang, L.-M.; Bulusu, S.; Zhai, H.-J.; Zeng, X.-C.; Wang, L.-S. *Angew. Chem., Int. Ed.* **2007**, *46*, 2915. (b) Wang, L.-M.; Pal, R.; Huang, W.; Zeng, X.-C.; Wang, L.-S. *J. Chem. Phys.* **2009**, *130*, 051101. (c) Wang, L.-M.; Bai, J.; Lechtken, A.; Huang, W.; Schooss, D.; Kappes, M. M.; Zeng, X.-C.; Wang, L.-S. *Phys. Rev. B* **2009**, *79*, 033413. (d) Zorriasatein, S.; Joshi, K.; Kanhere, D. G. *J. Chem. Phys.* **2008**, *128*, 184314. (e) Gao., Y.; Shan, N.; Pei, Y.; Zeng, X.-C. *Nano Lett.* **2010**, *10*, 1055.

(20) Brust, M.; Walker, M.; Bethell, D.; Schiffrin, D. J.; Whyman, R. J. *Chem. Soc., Chem. Commun.* **1994**, 801.

(21) Hostetler, M. J.; Zhong, C. J.; Yen, B. K. H.; Anderegg, J.; Gross, S. M.; Evans, N. D.; Porter, M. D.; Murray, R. W. *J. Am. Chem. Soc.* **1998**, *120*, 9396.

(22) Mott, D.; Galkowski, J.; Wang, L.; Luo, J.; Zhong, C. J. *Langmuir* **2007**, *23*, 5740.

(23) Buffat, P.; Borel, J. P. *Phys. Rev. A* **1976**, *13*, 2287.

(24) Oxford, S. M.; Lee, P. L.; Chupas, P. J.; Chapman, K. W.; Kung, M. C.; Kung, H. H. *J. Phys. Chem. C* **2010**, *114*, 17085.

(25) Petkov, V. *J. Appl. Crystallogr.* **1989**, *22*, 387.

(26) Egami, T.; Billinge, S. J. L. *Underneath the Bragg Peaks*; Pergamon Press: Amsterdam, 2003.

(27) Petkov, V. *Mater. Today* **2008**, *11*, 28.

(28) Wu, C.; Yin, M.; O'Brien, S.; Koberstein, J. T. *Chem. Mater.* **2006**, *18*, 6054.

(29) Ma, X.; Wang, G.; Yukimura, K.; Sun, M. *Surf. Coat. Technol.* **2007**, *201*, 6712.

(30) Motl, N. E.; Ewusi-Annan, E.; Sines, I. T.; Jensen, L.; Schaak, R. E. *J. Phys. Chem. C* **2010**, *114*, 19263.

(31) Malis, O.; Byard, C.; Mott, D.; Wanjala, B.; Loukrakpam, R.; Luo, J.; Zhong, C. J. *Nanotechnology* **2011**, *22*, 025701.

(32) Reinhard, D.; Hall, B. D.; Berthoud, P.; Valkealahti, S.; Monot, R. *Phys. Rev. Lett.* **1997**, *79*, 1459.

(33) Koga, K.; Ikeshoji, T.; Sugawara, K. I. *Phys. Rev. Lett.* **2004**, *92*, 115507.

(34) Schebarchov, D.; Hendy, S. C. *Phys. Rev. Lett.* **2006**, *96*, 256101.

(35) Rodríguez-López, J. L.; Montejano-Carrizales, J. M.; Pal, U.; Sánchez-Ramírez, J. F.; Troiani, H. E.; García, D.; Miki-Yoshida, M.; José-Yacamán, M. *Phys. Rev. Lett.* **2004**, *92*, 196102.

(36) Rodríguez-Lópeza, J. L.; Montejano-Carrizalesc, J. M.; José-Yacamán. *Appl. Surf. Sci.* **2003**, *219*, 56.

(37) Darby, S.; Mortimer-Jones, T. V.; Johnson, R. L.; Roberts, C. *J. Chem. Phys.* **2002**, *116*, 1536.

(38) Han, X. J.; Chen, M.; Guo, Z. Y. *J. Phys: Condens. Matter.* **2004**, *16*, 705.

(39) Loukrakpam, R.; Wanjala, B. N.; Yin, J.; Fang, B.; Luo, J.; Shao, M.; Protsailo, L.; Kawamura, T.; Chen, Y.; Petkov, V.; Zhong, C. J. *ACS Catal.* **2011**, *1*, 562.

(40) Wanjala, B.; Fang, B.; Loukrakpam, R.; Chen, Y.; Engelhard, M.; Luo, J.; Yin, J.; Yang, L.; Shan, S.; Zhong, C. J. *ACS Catal.* **2012**, *2*, 795.

(41) Yang, L.; Shan, S.; Loukrakpam, R.; Petkov, V.; Ren, Y.; Wanjala, B.; Engelhard, M.; Luo, J.; Yin, J.; Chen, Y.; Zhong, C. J. *J. Am. Chem. Soc.* **2012**, *134*, 15048−15060.